



Full Text View

[Volume 29, Issue 9 \(September 1999\)](#)

Journal of Physical Oceanography

Article: pp. 2382–2404 | [Abstract](#) | [PDF \(403K\)](#)

Rossby Wave–Coastal Kelvin Wave Interaction in the Extratropics. Part I: Low-Frequency Adjustment in a Closed Basin

Zhengyu Liu, Lixin Wu, and Eric Bayler

Department of Atmospheric and Oceanic Sciences, University of Wisconsin—Madison, Madison, Wisconsin

(Manuscript received May 12, 1998, in final form November 12, 1998)

DOI: 10.1175/1520-0485(1999)029<2382:RWCKWI>2.0.CO;2

ABSTRACT

The interaction of open and coastal oceans in a midlatitude ocean basin is investigated in light of Rossby and coastal Kelvin waves. The basinwide pressure adjustment to an initial Rossby wave packet is studied both analytically and numerically, with the focus on the low-frequency modulation of the resulting coastal Kelvin wave. It is shown that the incoming mass is redistributed by coastal Kelvin waves as well as eastern boundary planetary waves, while the incoming energy is lost mostly to short Rossby waves at the western boundary. The amplitude of the Kelvin wave is determined by two mass redistribution processes: a fast process due to the coastal Kelvin wave along the ocean boundary and a slow process due to the eastern boundary planetary wave in the interior ocean. The amplitude of the Kelvin wave is smaller than that of the incident planetary wave because the initial mass of the Rossby wave is spread to the entire basin. In a midlatitude ocean basin, the slow eastern boundary planetary wave is the dominant mass sink. The resulting coastal Kelvin wave peaks when the peak of the incident planetary wave arrives at the western boundary.

The theory is also extended to an extratropical–tropical basin to shed light on the modulation effect of extratropical oceanic variability on the equatorial thermocline. In contrast to a midlatitude basin, the fast mass redistribution becomes the dominant process, which is now accomplished mainly by equatorial Rossby and Kelvin waves, rather than the coastal Kelvin wave. The coastal Kelvin wave and the modulation of the equatorial thermocline peak close to the time when the wave trail of the incident Rossby wave arrives at the western boundary. Finally, the theory is also applied to the wave interaction around an extratropical island.

Table of Contents:

- [Introduction](#)
- [The theory](#)
- [Shallow-water model experiments](#)
- [Application to extratropical–tropical](#)
- [Summary and discussions](#)
- [REFERENCES](#)
- [APPENDIX](#)
- [FIGURES](#)

Options:

- [Create Reference](#)
- [Email this Article](#)
- [Add to MyArchive](#)
- [Search AMS Glossary](#)

Search CrossRef for:

- [Articles Citing This Article](#)

Search Google Scholar for:

- [Zhengyu Liu](#)
- [Lixin Wu](#)
- [Eric Bayler](#)

1. Introduction

In a midlatitude ocean basin, the two most important low-frequency waves are the Rossby wave and coastal Kelvin wave. Most previous works have focused on the Rossby wave. Long Rossby waves (or planetary waves) are important for the adjustment in the interior ocean, while short Rossby waves are responsible for the intensive current variability along the western boundary (e.g., [Pedlosky 1965, 1987](#); [Anderson and Gill 1975](#); [Cane and Sarachik 1977, 1979](#); [McCreary and Kundu 1988](#)). However, relatively less attention has been paid to the role of the coastal Kelvin wave and its interaction with Rossby waves in the low-frequency variability of the midlatitude ocean. In particular, there have been few studies on the interaction of Rossby waves and coastal Kelvin waves on the western boundary. When a Rossby wave incident is on the midlatitude western boundary, it is known that short Rossby waves are generated to balance the incoming cross-shore mass and energy fluxes ([Pedlosky 1987](#)). Coastal Kelvin waves will also be excited. However, the mechanism responsible for the coastal Kelvin wave is not fully understood. This will be the major question to be explored here.

The interaction of midlatitude Rossby and coastal Kelvin waves has at least three applications. First, it is an important process that contributes to the exchange of open and coastal ocean variability. Second, the coastal Kelvin wave generated by decadal planetary waves in the midlatitude may provide a mechanism for the modulation of the equatorial thermocline and therefore contributes to decadal climate variability in the subtropical–tropical climate system ([Lysne et al. 1997](#)). Third, this interaction, as will be seen later, is critical for the low-frequency variability of island circulation.

Previous works on the interaction of Rossby and Kelvin waves can be divided into three groups. The first group includes numerous studies that investigated the interaction of equatorial Kelvin wave and equatorial Rossby waves (e.g., [McCreary 1976](#); [Cane and Sarachik 1977, 1979](#); [Kawase 1987](#)). It is found that wave reflection is determined mainly by the balance of zonal mass transport. The alongshore mass distribution is accomplished by short Rossby waves, which contributes little to the zonal mass transport and therefore plays little role in determining the reflected Kelvin and long Rossby waves. These studies have laid the foundation to our understanding of seasonal- to interannual climate variability, such as the ENSO in the Pacific Ocean (e.g., [McCreary 1983](#); [Cane and Zebiak 1985](#); [Battisti 1989, 1991](#); [Kessler 1991](#)) and the Somali Current system in the Indian Ocean (e.g., [McCreary and Kundu 1988](#)). However, it will be seen later that interaction of the equatorial Rossby and Kelvin waves differs significantly from that between a midlatitude Rossby wave and a coastal Kelvin wave (see more discussions in [section 5](#)).

The second group focused on the extratropical ocean, but only along the eastern boundary. The primary issue is the generation of planetary waves by coastal Kelvin waves along the eastern boundary (e.g., [Enfield and Allen 1980](#); [White and Saur 1983](#); [Jacobs et al. 1994](#); [McCalpin 1995](#)). At low frequencies, coastal Kelvin waves change the eastern boundary pressure, which in turn generates planetary waves radiating westward into the interior ocean. These studies are important to understand the impact of annual to decadal variability of coastal upwelling on the interior ocean.

The third group investigated the interplay of midlatitude Rossby waves and coastal Kelvin waves, mostly along the western boundary. Most of these works originated from the issue of mass conservation (or the consistency condition) in a quasigeostrophic (QG) model in a midlatitude basin ([McWilliams 1977](#); [Flierl 1977](#); [Dorofeyev and Larichev 1992](#); [Millif and McWilliams 1994, hereafter MM](#)). All these works strongly suggested that the coastal Kelvin wave plays a key role in mass conservation. Our work is a further extension of these works. [Godfrey \(1975\)](#) and [McCreary and Kundu \(1988\)](#) have discussed some initial reflection processes and some local dynamics with the focus on low latitudes. Dorofeyev and Larichev limited their discussion to a half-plane midlatitude ocean, and therefore it does not directly apply to a closed basin. Kelvin wave propagation around a basin has also been discussed in numerical models ([Cane and Sarachik 1979](#); [McCreary 1983](#); MM). As will be seen later, the modulation of a coastal Kelvin wave is a nonlocal process due to the rapid propagation of the coastal Kelvin wave. Consequently, the response differs dramatically for different ocean basins. The modeling study of MM shows a remarkable resemblance between the shallow-water model and the quasigeostrophic model, after the consistency condition is imposed in the latter. This assures that the principle mechanisms for the interaction of Rossby and coastal Kelvin waves are contained in a QG system. However, in none of these works are the physical mechanisms, especially those responsible for the quantitative aspects of the wave interaction, fully studied.

We will investigate the basinwide adjustment process to an initial planetary wave packet incident on a midlatitude western boundary, with the focus on the quantitative aspects of the interaction. We will attempt to address the following questions: What is the magnitude of the slowly evolving coastal Kelvin wave, and when does it peak? What are the major factors that determine the strength and timing of the Kelvin wave amplitude? Furthermore, in a basin that includes the equator, what is the impact of the wave interaction in the midlatitude on the modulation of the equatorial thermocline? A simple analytical theory is first developed to determine the amplitude evolution of the coastal Kelvin wave. Extensive numerical experiments are performed to substantiate the theory. The modulation of the Kelvin wave is found to be determined by two nonlocal mass redistribution processes: one fast and the other slow. The former is due to the coastal Kelvin wave current, while the latter is attributed to the eastern boundary planetary wave. The amplitude evolution of the coastal Kelvin wave depends critically on the mass redistribution process. Different from the reflection of equatorial Rossby and Kelvin waves, which is determined by the balance of cross-shelf mass flux along the equator, the coastal Kelvin wave is generated to balance the

alongshore mass flux of the incident long Rossby wave in the midlatitude.

The paper is arranged as follows. A QG theory is developed in [section 2](#) to illustrate the major processes that determine the interaction between planetary waves and coastal Kelvin waves in a midlatitude basin. Supporting numerical experiments are carried out in a shallow-water model in [section 3](#). The theory is then extended to a combined extratropical–tropical basin in [section 4](#) to study the modulation of midlatitude planetary waves on the equatorial thermocline. A summary and a brief comparison with the interaction of equatorial Rossby and Kelvin waves are given in [section 5](#). Finally, a direct application of our theory to the wave interaction around an island is given in the appendix.

2. The theory

a. Model and solution

The modeling study of MM assures convincingly that the initial adjustment of Rossby and coastal Kelvin waves in a midlatitude ocean basin can be simulated in a QG model. Indeed, a low-frequency Kelvin wave can be approximated as an alongshore current because of its rapid along boundary propagation. This so-called coastal Kelvin wave current (CKC) is nearly geostrophic and can therefore be represented in a QG model. Mathematically, the speed of the Kelvin wave $c_o = (g'D)^{1/2}$ is independent of forcing frequency, where g' is the reduced gravity and D is the mean depth. Thus, along a straight coast, the alongshore wavenumber diminishes, $k = \omega/c_o \rightarrow 0$, as the forcing frequency vanishes ($\omega \rightarrow 0$). In other words, a low-frequency coastal Kelvin wave has a long alongshore wavelength and therefore resembles a coastal current. In a closed basin, this mathematical argument, although not strictly true, is still helpful. The adjustment time for the completion of a CKC around the basin is the traveling time of the Kelvin wave around the basin. For the first two baroclinic modes, c_o is no less than 1 m s^{-1} . Thus, the boundary adjustment time ranges from days to months and is less than half a year even for a basin of the size of the North Pacific Ocean.

As a first step, a linearized 1.5-layer QG model will be used to study the interaction between the Rossby wave and coastal Kelvin wave in a midlatitude basin. Mean advection and nonlinearity are not included at this stage. The most serious impact of the mean boundary current advection is likely to be on slow short Rossby waves, although coastal Kelvin waves may also be affected. Since short Rossby waves contribute little to the mass redistribution—the key process that determines the modulation of the coastal Kelvin wave, the absence of mean boundary current advection may not affect our conclusion on the coastal Kelvin wave significantly. The equation can be written in terms of sea surface height (SSH) h as

$$\partial_t(\nabla^2 h - h/d^2) + \beta \partial_x h = -r \nabla^2 h, (1a)$$

where $d = c_o/f_0$ is the deformation radius, $c_o = (gD\Delta\rho/\rho)^{1/2}$ is the gravity wave speed, and D is the mean thickness of the upper moving layer. A linear momentum damping is also used.¹ The boundary condition is no normal flow across the boundary

$$h|_{\partial\Omega} = K(t), (1b)$$

where $K(t)$ will be determined by mass conservation—a key point to be returned to later.

Following MM, the total SSH (h) can be decomposed into two parts: the Rossby wave part (h_R) and the Kelvin wave part (h_K):

$$h = h_R + h_K. (2)$$

The Rossby wave satisfies the QG equation

$$\partial_t(\nabla^2 h_R - h_R/d^2) + \beta \partial_x h = -r \nabla^2 h (3a)$$

within the basin and has no pressure anomaly around the basin boundary $\partial\Omega$:

$$h_R|_{\partial\Omega} = 0. (3b)$$

The Kelvin wave has an amplitude $K(t)$ and a fixed spatial structure $h^*(x, y)$:

$$h_K = K(t)h^*(x, y), (4)$$

where

$$\nabla^2 h^* - h^*/d^2 = 0, \quad h^*|_{\partial\Omega} = 1. (5)$$

Equation (5) implies that the Kelvin wave makes no contribution to local potential vorticity—a feature that can be verified directly for a shallow-water Kelvin wave along a straight coast on an f -plane. The implication is that the interaction between the Kelvin and planetary wave is not caused by potential vorticity flux.

The structure of the CKC can be derived using the standard boundary layer method (Pedlosky 1987). In the following, we will only consider a rectangular basin of $0 \leq x \leq X$ and $Y_S \leq y \leq Y_S + Y$ (see Fig. 1). The boundary layer solution of the CKC is then derived from (5) as

$$h^* = e^{-x/d} + e^{-(X-x)/d} + e^{-(y-Y_S)/d} + e^{-(Y_S+Y-y)/d}, (6)$$

where the first through fourth terms on the rhs represent the CKC along the western, eastern, southern, and northern boundaries, respectively. This is a coastal current of width d , or the CKC. Here a small correction due to corners (at the order of $d/L \ll 1$) is neglected as in the Fofonoff basin mode (Fofonoff 1954). This neglect seems to be justified based on the numerical simulation of MM, which shows an insignificant effect of the corner on the modulation of the boundary pressure. The small effect of the corner has also been discussed in the case of an inertial western boundary current by Liu (1990).

Now we derive a basin solution for the adjustment in response to an initial planetary wave packet

$$h = h_i(x + Ct, y), (7)$$

where $C = \beta d^2$ is the speed of the planetary wave. The planetary wave satisfies

$$\partial_t(-h_R/d^2) + \beta \partial_x h = 0 (8)$$

in the interior ocean. In addition, the Kelvin wave vanishes in the interior ocean according to (6), leading to $h = h_R$. For the long wave in (8), we have assumed a weak dissipation such that the dissipation timescale ($1/r$) is much longer than that of the planetary wave ($x_p/\beta d^2$). For an initial planetary wave packet of zonal scale $x_p \gg d$, this requires $1 \ll (1/r)/(x_p/\beta d^2) = d^2/\delta x_p$, where $\delta = r/\beta$ is the width of the Stommel boundary layer. Therefore, the dissipation effect on long waves is negligible if $\delta/d \ll d/x_p \ll 1$.

The planetary wave first reaches the western boundary, where Eq. (1a) can be reduced to the western boundary layer equation:

$$\beta \partial_x h = -r \partial_{xx} h (9)$$

on the western boundary layer.

Here we have assumed that reflected short Rossby waves are damped within the boundary layer in a timescale ($1/r$) much shorter than that of the short Rossby wave adjustment (T_{bdry}). The temporal variability term in (1) can be shown negligible with $\delta/d \ll 1$. The resulting boundary layer pressure field has a quasi-steady-state response (9). The western boundary layer solution has to satisfy the no-normal flow boundary condition (1b). In addition, it has to match the incident wave in the interior as

$$h \rightarrow h_i(x + Ct, y)|_{x=0} = h_i(Ct, y) \text{ as } x/\delta \rightarrow \infty. (10)$$

The western boundary layer solution can therefore be derived as

$$h = h_i(Ct, y)(1 - e^{-x/\delta}) + K(t)e^{-x/\delta}; 0 < x/\delta < \infty,$$

where we have used [Eqs. \(2\)](#), [\(3b\)](#), [\(5\)](#), and [\(10\)](#). Thus, the solution in the entire western part of the basin (see [Fig. 1](#)) can be written as

$$h_W = h_{WL} + h_{WS} + h_{WK}, \quad 0 < x < x_p - Ct, \quad (11a)$$

where

$$h_{WL} = h_i(x + Ct, y), \quad h_{WS} = -h_i(Ct, y)e^{-x/\delta}, \quad h_{WK} = K(t)e^{-x/\delta}. \quad (11b)$$

Here h_{WL} is the incident planetary wave, h_{WS} is the damped reflected short Rossby wave, and h_{WK} is the sum of the CKC along the western boundary $K(t)e^{-x/d}$ [see [\(6\)](#)] and the damped short Rossby wave that is forced by the western boundary Kelvin wave $K(t)(e^{-x/\delta} - e^{-x/d})$ [see [Liu et al. \(1999\)](#) for further discussions]. Note that the spatial structure of the total response to the Kelvin wave forcing along the western boundary (h_{WK}) is determined by the viscous boundary layer scale δ , which is independent of the structure of the Kelvin wave having a deformation radius d . The h_{WK} solution is similar to the Kelvin–Munk wave of [Godfrey \(1975\)](#) where he used a no-slip boundary condition.

Along the southern and northern boundaries ([Fig. 1](#)), there are no reflected Rossby waves. Thus, the solutions in the southern and northern boundaries consist only of the CKCs [note [\(6\)](#)]:

$$h_S = K(t)e^{-(y-Y_s)/d}, \quad 0 < (y - Y_s)/d < \infty \quad (12)$$

$$h_N = K(t)e^{-(Y_s+Y-y)/d}, \quad -\infty < (y - Y - Y_s)/d < 0. \quad (13)$$

Here we assumed that the pressure anomaly of the incident planetary wave vanishes in both the southern and northern boundary layers. Otherwise, an additional diffusive boundary layer need to be added ([Pedlosky et al. 1997](#)).

Along the eastern boundary there is no viscous boundary layer; therefore, the solution consists of a planetary wave that radiates away from the eastern boundary. This wave should satisfy the planetary wave [equation \(8\)](#) and, consequently, should have the form of $h_E(x + Ct)$. The boundary condition [\(1b\)](#) requires $h_E(X + Ct) \equiv K(t)$ along the eastern boundary. Therefore, the solution in the eastern part is

$$h_E = K[t + (x - X)/C], \quad X - Ct < x < X. \quad (14)$$

Notice that the two diffusive boundary layers on the northern and southern boundaries have been neglected in [\(14\)](#). The h_E is dominated by an eastern boundary planetary wave (EBP). It can be considered as the sum of the forced planetary wave $K[t + (x - X)/C] - K(t)e^{-(X-x)/d}$ and the CKC along the eastern boundary $K(t)e^{-(X-x)/d}$ in [\(6\)](#). Solution [\(14\)](#) can be shown to be the low-frequency limit in a generalized QG equation ([McCalpin 1995](#); [Liu et al. 1999](#)). Thus, except for the unknown amplitude $K(t)$ of the CKC, Eqs. (11)–(14) give the complete basin solution, valid until the EBP reaches the western boundary, or $t < X/C$.

b. Mass conservation and Kelvin wave amplitude

The CKC amplitude is determined by total mass conservation $\partial_t M \equiv \partial_t \iint_{\Omega} h \, dx \, dy = 0$ ([Godfrey 1975](#); [McWilliams 1977](#); [Flierl 1977](#); [Dorofeyev and Larichev 1992](#); MM). In the following, the incident planetary wave is assumed to arrive at the western boundary at $t = 0$ and is of the form ([Fig. 1](#))

$$h_i(x, y) = h_0 \sin(\pi x/x_p) \cos[\pi(y - Y_c)/y_p],$$

$$\text{for } 0 \leq x \leq x_p,$$

$$-0.5y_p \leq y - Y_c \leq 0.5y_p \quad (15a)$$

$$h_i(x, y) = 0 \quad \text{elsewhere,} \quad (15b)$$

where the initial amplitude is h_0 , and the center latitude of the initial pulse is $Y_c = Y_S + 0.5Y$. The initial mass is therefore

$$m_o = \iint_{\Omega} h_i dx dy = (2x_p/\pi)(2y_p/\pi)h_0, \quad (16)$$

where the factor $2/\pi$ arises from the integral of the half-sine profile.

The mass in the western region is contributed by the incident long wave (M_{WL}), the reflected damped short wave (M_{WS}), and Kelvin wave (M_{WK}) [per (11)]:

$$M_w = \int_{Y_S}^{Y_S+Y} dy \int_0^{x_p-Ct} h_w dx = M_{WL} + M_{WS} + M_{WK}. \quad (17a)$$

Using the h_{WL} , h_{WS} , and h_{WK} in (11b), one can show that

$$M_{WL} = 0.5m_o[1 + \cos(Ct\pi/x_p)]H(x_p - Ct) \quad (17b)$$

$$M_{WS} = 0.5m_o[-q \sin(Ct\pi/x_p)]H(x_p - Ct) \quad (17c)$$

$$M_{WK} = K(t)Y\delta, \quad (17d)$$

respectively, where $q = \delta\pi/x_p$ and H is the Heaviside function: $H(z) = 1$ for $z \geq 0$ and $H(z) = 0$ for $z < 0$. Clearly, the mass of the short Rossby wave M_{WS} is negligible compared with the incident planetary wave M_{WL} as long as $x_p \gg \delta$. Along the southern and northern boundaries, the mass is due to CKCs (12) and (13) as

$$M_S = \int_{Y_S}^{Y_S+Y} dy \int_0^X h_S dx = K(t)Xd$$

and

$$M_N = \int_{Y_S}^{Y_S+Y} dy \int_0^X h_N dx = K(t)Xd. \quad (18)$$

Finally, the mass in the eastern region is dominated by the EBP and can be derived from (14) as

$$M_E = \int_{Y_S}^{Y_S+Y} dy \int_{X-Ct}^X h_E dx = CY \int_0^t K(t') dt'. \quad (20)$$

Therefore, the amplitude $K(t)$ is determined by the total mass conservation

$$M_w + M_S + M_E + M_N = m_o. \quad (21)$$

The mass source M_w is redistributed by two processes: M_N and M_S represent the fast mass redistribution process due to CKC along the northern and southern coasts (M_{WK} is also a fast process), while M_E represents a slow mass redistribution process toward the interior ocean by the EBP. The fast process redistributes mass over the entire coastal region, which has a width d and, therefore, a fixed area. The slow process, however, redistributes mass over an area that slowly expands westward. It will be seen that the evolution of the CKC amplitude $K(t)$ is determined predominantly by these two mass redistribution processes.

The mass conservation (21) can be differentiated to yield an ordinary differential equation

$$\frac{dK}{dT} + bK(T) = a[\sin(\pi T) + q \cos(\pi T)]H(1 - T) \quad (22a)$$

with the initial condition of

$$K(0) = 0. \quad (22b)$$

Here we have used the normalized quantities

$$T = \frac{Ct}{x_p}, \quad b = \frac{Yx_p}{\pi(2Xd + Y\delta)},$$

$$a = \frac{m_0}{2(2Xd + Y\delta)}. \quad (23)$$

The time

$$T_{EI} = 1 \quad (24a)$$

is the time when the incident long wave trail just reaches the western boundary (end time hereafter), and the time

$$T_{PI} = 0.5 \quad (24b)$$

is the time when the peak of the incident wave reaches the western boundary (peak time hereafter). The nondimensional parameter b (except for a factor π) is the area ratio of the final EBP area Yx_p and the CKCs area along the southern, northern, and western boundaries $2Xd + Y\delta$. This is an important parameter, because it measures the relative importance of the slow (EBP) and fast (CKC) processes. Finally, a is proportional to the ratio of the initial perturbation area to the coastal wave area. The amplitude $K(t)$ can be derived from (22) as

$$K(T) = \frac{a}{1 + b^2} \{e^{-b\pi T} - \cos(\pi T) + b \sin(\pi T) + q[b(\cos(\pi T) - e^{-b\pi T}) + \sin(\pi T)]\}$$

for $T \leq 1$ (25a)

$$K(T) = K(1)e^{-b\pi T} \equiv \frac{2adX(1 + e^{-b\pi})}{1 + b^2(2Xd + Y\delta)} e^{-b\pi T}$$

for $T > 1$. (25b)

The complete basin adjustment solution is therefore given by regional solutions in (11), (12), (13), (14), and the amplitude (25).

c. Mass exchange and modulation of CKC

Figures 2a–d plot four snapshots during an adjustment process in a basin of $X = 20^\circ$ and $Y = 20^\circ$, where $1^\circ = 111$ km. Other parameters are $\Delta\rho/\rho = 0.002$, $f_o = 7.3 \times 10^{-5} \text{ s}^{-1}$, $\beta = 2 \times 10^{-11} \text{ m}^{-1} \text{ s}^{-1}$, and $D = 500$ m. These parameters give a Stommel boundary layer width of $\delta = 19$ km and a deformation radius of $d = 44$ km. Zonal and meridional sections of the four snapshots are also plotted along the central latitude (Fig. 3a) and longitude (Fig. 3b), respectively. A planetary wave patch (of size $x_p = 10^\circ$, $y_p = 10^\circ$) is initiated near the western boundary at $T = 0$ (Fig. 2a) and circle-connected lines in Figs. 3a,b. At the peak time, $T_{PI} = 1/2$ (Fig. 2b) and solid lines in Figs. 3a,b, half of the patch has moved out of the western boundary, a sharp viscous boundary layer is formed along the coast, a significant CKC is

established around the basin, and an EBP radiates into the eastern ocean. At the end time $T_{EI} = 1$ (Fig. 2c and dash-dot lines in Figs. 3a,b), the initial perturbation planetary wave has just passed the western boundary and only a weak short Rossby wave (forced by CKC) exists. Around the coast, the CKC weakens, yet is still visible. On the east, the EBP has left the coast. Finally, at $T = 1.5$ (Fig. 2d and dashed lines in Figs. 3a,b), the CKC has virtually disappeared along all boundaries and the EBP has propagated to the middle basin. All of the major features of our theoretical solution closely resemble the QG model experiment of MM. One difference is that the initial wave packet in the QG model also generates dispersive waves that trail the leading wave packet. In addition, in the shallow-water model, the planetary wave front propagates faster at lower latitudes due to decreases in the Coriolis parameter.

The evolution of the CKC amplitude $K(T)$ is plotted in Fig. 4a (solid line). For comparison, the SSH variation of the incident planetary wave at the western boundary [$h_{WL}(0^\circ, 30^\circ)$] is also plotted (dotted line). It is seen that the $K(T)$ maximum is about 0.3 times the initial anomaly and is achieved at about $T = 0.58$, slightly after $T_{PI} = 0.5$.

The mass exchange among various wave components is shown in Fig. 4b. The mass of the incident long wave (solid line) decreases monotonically, losing all the mass at the end time $T_{EI} = 1$. The mass loss is little affected by the damped short Rossby wave (dotted line). Instead, most mass is initially lost to the CKC along the southern, northern, and western boundaries (dash-dot). Later, most mass leaks into the EBP (dashed line), which eventually completely absorbs the initial mass. Therefore, in this case, $K(T)$ is determined predominantly by the slow transfer from the incident planetary wave to the expanding EBP, as shown in Fig. 4b.

d. Slow and fast mass redistribution

The mass balance for slow redistribution occurs between the incident planetary wave and the EBP:

$$M_{WL} + M_E = m_0, \quad \text{slow mass redistribution. (26)}$$

This mass balance, together with (17) and (20), leads to the amplitude

$$K(T) = \frac{dM_{WL}}{dT} = \frac{a}{b} \sin(\pi T) H(1 - T),$$

$$\text{for } 0 < T < \frac{X}{x_p}. \quad (27)$$

The maximum amplitude is therefore

$$K_M = \frac{a}{b} = \frac{m_0}{2x_p Y / \pi} = \frac{2}{\pi} \frac{y_p}{Y} h_o \leq h_o, \quad (28a)$$

or

$$\frac{m_0}{2K_M x_p Y / \pi} = 1. \quad (28b)$$

Equation (28b) states that the maximum amplitude is such that the total initial mass is completely converted to that of the EBP that has an amplitude K_M and an area $x_p Y$. In x direction, both the initial and final planetary waves have the same width x_p and the same shape (a half sine patch). Therefore, K_M is determined only by the ratio of the widths of the two waves in y direction as shown in (28a). The $2/\pi$ factor arises from the half sine shape in y for the initial wave, which differs from the eastern boundary wave that always has a uniform sea level in y as shown in (14).

The amplitude in (27) first increases to its maximum at the peak time $T_M = T_{PI} = 0.5$, then decreases to zero at the end time $T_{EI} = 1$ and remains unchanged thereafter. This behavior is similar to the example in Fig. 4a (solid line), which has $K_M \approx 0.31$, slightly smaller than the $1/\pi \approx 0.32$ estimated from (28), and which has $T_M \approx 0.58$, slightly later than the peak time $T_{PI} = 0.5$.



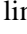
The fast mass redistribution may also be important in determining the amplitude evolution $K(t)$, as will be seen later in [section 4](#) for the case of a combined extratropical–tropical ocean basin. The evolution of $K(t)$ that is driven by the fast process differs significantly from that by the slow process. Indeed, if the mass is completely redistributed by the fast process along the northern and southern boundaries (neglecting friction so $q = 0$),

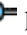


$$M_W + M_S + M_N = m_0, \quad \text{fast mass redistribution. (29)}$$

The amplitude can be derived as

$$K(T) = a[1 - \cos(\pi T)] \quad \text{for } T \leq 1 \quad (30a)$$

$$K(T) = 2a \quad \text{for } 1 < T \leq X/x_p. \quad (30b)$$

Now, $K(T)$ continues to increase until the end time and remains unchanged thereafter, so $T_M = 1$. The dashed line ($b = 0$ curve) in [Fig. 4a](#)  illustrates this response. This evolution is in sharp contrast to the slow process discussed above, where $T_M = 0.5$. The different peaking time for fast and slow mass redistribution can be understood as follows. In the absence of an EBP, the CKC can only redistribute mass to a fixed coastal area (of width d on the southern, and northern, and δ on the western boundaries).² Therefore, as the incident wave injects more mass into the Kelvin wave, the amplitude of the CKC increases. The maximum amplitude is therefore achieved at the end time, when all the incident mass is accumulated to the CKC. As shown in [Fig. 4c](#) , the decreasing mass of the incident planetary wave (solid line) is balanced completely by the increasing mass in the CKC (dash–dot line). In contrast, when the slow process becomes important ([Fig. 4b](#) ) , as time progresses, the continued addition of mass to the CKC is offset by an increasing area due to the slow westward expansion of the EBP. This offset precludes an increase of amplitude. In the extreme case, when all the mass is redistributed by the slow process, as in [\(26\)](#), $K(T)$ reaches its maximum at $T_{PI} = 0.5$ when the *rate* of incident mass reduction is the greatest [see [\(27\)](#)].

The relative importance of the slow EBP versus the fast CKC processes is measured by the area ratio parameter b in [\(23\)](#). A large (small) b favors the slow (fast) process. The solutions for the complete slow and fast redistributions [[\(27\)](#) and [\(30\)](#), respectively] are the asymptotic solutions of the full solution [\(25\)](#) in the limits of $b \rightarrow \infty$ and $b \rightarrow 0$, respectively (neglecting friction). [Figure 5](#)  plots the time of maximum amplitude T_M as a function of b . In general, T_M is later than $T_{PI} = 0.5$, but earlier than $T_{EI} = 1$ due to the competition between the fast and slow processes. If the slow process dominates (large b), T_M is closer to $1/2$, and vice versa. Even for a modestly large b ($b = 2$), T_M is already fairly close to $1/2$. The example of [Fig. 4b](#)  has $b \approx 5.7$; therefore, its evolution (solid line in [Fig. 4a](#) ) resembles the slow process. In an extratropical basin, $b \gg 1$ is usually true because the EBP has an area comparable to the basin area, while the CKC has an area of subbasin scale due to the narrow offshore width d . However, if the equatorial region is included, the dominant role of EBP will no longer be true, as will be discussed in [section 4](#).

e. Energetics

The slow EBP process and the fast CKC process are the two major mass sinks and, therefore, determine the modulation of the CKC. However, neither of them is the dominant energy sink of the initial long wave disturbance. Instead, most of the initial energy is converted in the western boundary to the kinetic energy of the short Rossby wave ([Pedlosky 1965](#)), which, because of its dispersive nature and the small area occupied, plays little role in the mass balance. The consistency of the mass and energy balances can be understood as follows. First, we notice that the energy of the QG model, after neglecting a constant factor, is

$$E = (\partial_x h)^2 + (\partial_y h)^2 + (h/d)^2,$$

where the first two terms are the kinetic energy and the last term is the available potential energy (APE). The initial mass and energy (mainly APE) of the incident planetary wave are at the order of

$$M_0 \sim A_0 h_0, \quad E_0 \sim A_0 (h_0/d)^2, \quad (31)$$

where $A_0 = x_p y_p$ is the initial area and h_0 is the initial amplitude. Eventually, the EBP has the mass and energy (again mainly APE) of

$$M_E \sim A_E K, \quad E_E \sim A_E (K/d)^2, \quad (32)$$

where $A_E = x_p Y$ is the area of the EBP. Mass conservation of the initial and final flow field requires $M_0 \sim M_E$, or, with (31) and (32), $K \sim (A_0/A_E)h_0$. Therefore, the final energy of the EBP is $E_E \sim A_E[(A_0/A_E)h_0/d]^2 \sim (A_0/A_E)E_0$. Since the area of the initial wave cannot be larger than the basin, $A_0/A_E = y_p/Y \leq 1$, we have $E_E \leq E_0$. Thus, as long as the initial pulse occupies an area smaller than the basin scale, the energy of the EBP is always smaller than the initial energy and, therefore, cannot be the dominant energy sink. Physically, although the initial mass is transmitted to the EBP, the larger area of the EBP reduces the response amplitude and, in turn, the center of gravity. Consequently, part of the APE is lost. This energy loss can be seen clearly in Fig. 6, the energy evolution diagram for the example in Fig. 2. The energy associated with the incident planetary wave (E_W) decreases monotonically, vanishing at about the end time 1. The energy of the EBP (E_E) increases monotonically, but reaches a final energy level that is much smaller than the initial disturbance energy level. The CKC energy (E_K) is even less than the EBP in the later stage of the evolution. The remaining energy is lost mainly to the short Rossby wave along the western boundary. Since the short Rossby wave is associated principally with the kinetic energy of the western boundary current, its energy should dominate the kinetic energy of the western region (E_W). However, in our viscous case (1), the damped short Rossby wave (17c) has the area integrated energy within the viscous boundary layer (mainly kinetic energy from the alongshore current) of $E_W \sim (h_0/\delta)^2 y_p \delta \sim (d/x_p)(d/\delta)E_0$. For an incident planetary wave that is much wider than the deformation radius ($d \ll x_p$), the damped short wave energy is much smaller than the initial energy $E_W \ll E_0$. This difference can be seen in the kinetic energy (circles) for the western region, diagrammed in Fig. 6. In the presence of dissipation, the total energy (E_{Total}) is reduced as shown in Fig. 6.

In an inviscid case, however, the lost energy of the incident long wave can be absorbed by the reflected short Rossby waves. To estimate the area integrated kinetic energy of the short Rossby wave, we notice that the area occupied by the short Rossby wave has the meridional extent y_p and the zonal extent of $C_g T_b$, where $C_g \sim \beta/k^2$ is the group velocity of the short Rossby wave, $T_b \sim x_p/C$ is the time for the incident planetary wave to pass through the western boundary, and $k \sim 1/\delta$ is the dominant short zonal wavenumber. The energy of the short Rossby wave is then on the order of $E_{WS} \sim (h_0 k)^2 C_g T_b y_p \sim (h_0/d)^2 x_p y_p \sim E_0$. Thus, the initial energy can be converted completely to the kinetic energy of the short Rossby wave. This discussion also helps to understand the QG model in which, if one only considers Rossby waves, the energy is conserved, but not the mass.

In short, our study above suggests that the incident planetary wave first loses its mass to CKC. Along the eastern boundary, the Kelvin wave sheds mass into a planetary wave, generating an EBP. Available energy is reduced compared to the initial energy because of the EBP's smaller amplitude, which is caused by the spreading of the EBP. Instead, most of the incident energy is lost to the short Rossby wave along the western boundary. In spite of its importance in energy balance, the short Rossby wave contributes little to mass redistribution and, therefore, has little impact on the modulation of the CKC. The EBP balances most of the mass and determines the modulation of the CKC.

3. Shallow-water model experiments

Here, we present numerical experiments to further substantiate our theory. The model is a 1.5-layer shallow-water model on a beta plane (Wallcraft 1991). The horizontal resolution is $1/8^\circ$. The control run has the model configuration and parameters the same as those of the analytical solution in Fig. 2. The coefficient of Laplacian diffusion is $140 \text{ m}^2 \text{ s}^{-1}$, which gives a Munk boundary layer width 19 km, the same as the Stommel boundary layer width in the case of Fig. 2. The initial SSH is also chosen to be the same form as (15), and the initial currents are in geostrophic balance. The initial amplitude is small so that the solution is essentially linear.

Figure 7 shows four snapshots of SSH, and Fig. 8 shows the SSH profiles along the zonal and meridional midbasin sections (all SSH are normalized by the amplitude of the initial perturbation wave). Overall, the shallow-water solutions in Figs. 7 and 8 resemble closely the corresponding QG theoretical solutions in Figs. 2 and 3, respectively. There are also two differences. First, the initial shallow water wave has a weak dispersion during its westward propagation—a feature that also exists in the QG model simulation of MM. Second, the planetary wave propagates faster at lower latitudes. This feature can be simulated in a generalized QG model if the wave speed is allowed to vary with latitude (McCalpin 1995) and therefore can be readily included in our theory.

The evolution of the CKC in Fig. 9a closely resembles that in the theoretical QG solution in Fig. 4a. For reference, the time series of midlatitude SSH outside the western boundary layer at $(0.6^\circ, 30^\circ\text{N})$ is used to calculate the proxy for the SSH amplitude evolution of the incident planetary wave on the western boundary (dot in Fig. 9a) corresponding to h_{WL}

(0° , 30°N) in the QG theory (dotted line in Fig. 4a). The theoretical peak and end times of the incident wave can be calculated as $0.5x_p/C = 180$ days and $x_p/C = 360$ days, respectively. These correspond roughly to the peak and end times of the western boundary SSH [$h_{WL}(0^\circ, 30^\circ\text{N})$ in Fig. 9a]. The evolution of the CKC can be seen in the coastal SSHs on the southern (solid), eastern (star), northern (plus), and western (circle) boundaries (Fig. 9a). The coastal SSHs evolve with virtually the same amplitude and phase, although the amplitude is slightly larger on the western coast. This supports the speculation that a low-frequency coastal Kelvin wave has a uniform SSH along the coast, as assumed in (1b). The coastal SSHs in Fig. 9a, therefore, correspond to $K(t)$ —the amplitude of CKC in the theory (solid line in Fig. 4a). The maximum amplitude is $K_M \approx 0.26$ for the shallow-water case (Fig. 9a), slightly less than the theoretical value $K_M \approx 0.3$ (Fig. 4a). The maximum occurs at about $T_M = 190$ days in the shallow water case (Fig. 9a), corresponding to a nondimensional $T_M = 0.54$, close to the theoretical value $T_M = 0.57$ (Fig. 4a).

The mass exchange process and energetics are also similar between the shallow-water model (Figs. 9b,c) and the QG theory (Figs. 4b and 6). Figure 9b plots the mass evolution of the western region [M_W as in (11a)] that is dominated by the incident long wave, the EBP (M_E), and the CKC along the southern and northern boundaries ($M_N + M_S$). As in the theory (Fig. 4b), the mass of the incident wave decreases monotonically until the end time about day 300. Initially, the mass loss to the CKC and EBP is comparable, but the mass loss to the EBP dominates in the later stage. A comparison of the theoretical solution, Fig. 4b, with the shallow-water solution, Fig. 9b, reveals a somewhat stronger CKC in the shallow-water case, especially in the later stage after day 400. This difference is due to a more realistic EBP in the shallow-water model. First, the EBP front is accompanied by a meridional current that intersects the southern and northern boundaries, forcing CKCs there. Second, in the later stage, the faster EBP front in the southern basin reaches the western boundary (Fig. 7d), generating an additional CKC.

The energy evolution of the shallow-water solution is plotted in Fig. 9c for the same three components as the mass. For each component, both the total energy (solid line with marks) and the kinetic energy (unconnected marks) are plotted. It is seen that the initial energy in the western region (E_W) is lost rapidly, initially to the CKC ($E_N + E_S$) and then to the EBP (E_E). There is a small amount of kinetic energy in the western region, mostly due to the damped short Rossby wave: the CKC kinetic energy is about half the total energy, while the EBP kinetic energy is negligible, as they should be. All of the features agree with the theory (Fig. 6) remarkably well.

Finally, sensitivity experiments are performed for various sizes and locations of the initial anomaly. Figure 10 presents the normalized maximum amplitude (K_M) (Figs. 10a,c) and time of maximum (T_M) (Figs. 10b,d) CKC amplitude for four sets of sensitivity experiments. The first set has seven experiments (pluses in Figs. 10a,b) in which the initial patches are all centered in the middle of the basin ($x = 10^\circ$, $y = 30^\circ\text{N}$) but have different zonal widths; the second set also has seven experiments (pluses in Figs. 10c,d), which are the same as the first set, except that meridional sizes are varied; the third set has four experiments (stars in Figs. 10a,b), which are the same as the first set, but the initial patch has its western edge on the western boundary; the fourth set has four experiments (stars in Figs. 10c,d), which are the same as the third set except with different meridional widths. The experiments with varying zonal size (Figs. 10a,b) all have $y_p = 6^\circ$, while the experiments with varying meridional size (Figs. 10c,d) all have $x_p = 6^\circ$. The corresponding theoretical QG solutions are also plotted in Fig. 10 (circles). It is seen that the model and theory have a good overall agreement, with the error usually within about 20%. The agreement is particularly good for the two sets of experiments with the initial patch against the western boundary (stars) because of the small wave dispersion during the initial wave propagation toward the western boundary. The major features of the theoretical solution are clearly captured. For example, the amplitude does not change much with the zonal size (Fig. 10a), but increases linearly with the meridional size (Fig. 10c). This result is easy to understand, because, for the extratropical basin case, the dominant mass redistribution is the slow process due to the EBP. Therefore, the amplitude is determined, to first order, by the ratio of the meridional size y_p/Y , but independent of x_p , as shown in (28a). Overall, the theory tends to agree better with experiments of larger x_p . This is expected because of the role of the long wave approximation in the theory.

In short, our theory and model experiments suggest that in an extratropical basin the CKC is modulated mainly by the slow mass spreading of the EBP. As a result, the amplitude of CKC is weaker than the initial pulse, and the maximum is achieved slightly after the peak time of the incident wave. Most of the initial energy is lost to short Rossby waves, which are then dissipated on the western boundary. Finally, it is important to point out that our theory, although derived in an extratropical basin, can be applied directly to the adjustment process around an island. This will be discussed in the appendix. Furthermore, it can be shown that the formation of an island circulation (Godfrey 1989) can be clearly understood in terms of the interaction of coastal Kelvin waves and Rossby waves (Liu et al. 1999).

4. Application to extratropical–tropical interaction

The QG theory discussed above, after some modifications, can also be applied to a basin of combined extratropics–tropics with the inclusion of the equator. For the application to decadal climate variability (Lysne et al. 1997), it is important to keep in mind that we are studying the slow decadal modulation of the equatorial thermocline, rather than the fast (intraannual) equatorial waves. First of all, we should realize that, in a combined extratropical–tropical basin, the fast mass redistribution involves not only coastal Kelvin waves but also equatorial Kelvin and Rossby waves, all of which propagate with a speed comparable to that of the coastal Kelvin wave c_0 . The slow process, however, is still due to the extratropical EBP, now at decadal timescale. Along the western boundary, an equatorward coastal Kelvin wave will first be converted to an eastward equatorial Kelvin wave, which is then reflected on the eastern boundary by shedding most its mass and energy into a westward equatorial Rossby wave (Cane and Sarachik 1977, 1979). The Rossby wave then reflects as an equatorial Kelvin wave and so forth. These reflections of equatorial waves rapidly build up an equatorial quasi-basin mode (Cane and Moore 1981). A small amount of mass leaks out poleward along the eastern boundary in each hemisphere as a coastal Kelvin wave. The Kelvin wave then generates the EBP in the extratropics (Miles 1972; Enfield and Allen 1980; White and Saur 1981; Jacobs et al. 1994; McCalpin 1995). These fast processes in an combined extratropical–tropical basin will be referred to as the “Equatorial–Coastal Kelvin Wave Current” (ECKC), although one should keep in mind that equatorial Rossby waves are also included.

The conceptual model that we obtained in a midlatitude basin can be generalized to a combined extratropical–tropical basin. The major modification is to replace the coastal Kelvin waveguide (equator side) width of d for the equatorial region of fast mass redistribution due to equatorial waves. Realizing that the so-called fast or slow process is relative to the adjustment of the initial long wave, the latitude width y_E of the fast equatorial region (Fig. 11) can be estimated as follows. First, the equatorial region has to adjust faster than the incident extratropical planetary wave. Second, the slowest process in the equatorial region is the eastern boundary planetary wave radiating at y_E . Therefore, for this wave to be a part of the fast redistribution process, this wave must cross the basin width X at the speed $\beta g'D/f^2(y_E)$ by the time the initial midlatitude planetary wave (centered at latitude Y_c) passes the western boundary after traveling x_p at the speed of $\beta g'D/f^2(Y_c)$; that is,

$$\frac{X}{f^{-2}(y_E)} = \frac{x_p}{f^{-2}(Y_c)}.$$

The latitude width of the fast equatorial region is therefore determined by

$$f(y_E) = f(Y_c)(x_p/X)^{1/2}. \quad (33)$$

For a large-scale initial pulse in the midlatitude, this width is usually much larger than the deformation radius in the extratropics (d) or in the equator ($d_{EQ} = [(g'D)^{1/2}/\beta]^{1/2}$).³ This implies that, if an extratropical basin is extended to include the equator, the amplitude of the ECKC will be reduced due to the spreading of the initial mass into a larger area. Furthermore, the time of maximum ECKC should be delayed closer to the end time T_{EF} . This is because the increased area is contributed predominantly by the equatorial region, which has a fast mass redistribution. Therefore, the area that the fast process occupies is significantly increased relative to the slow process. The mass balance should resemble more the fast process (29) than the slow process (26) of an extratropical basin. These speculations are confirmed by the shallow-water experiments below.

The major features of the adjustment process in a combined extratropical–tropical basin are demonstrated in the shallow-water experiment illustrated by Figs. 12 and 13, which should be compared with the corresponding figures for the extratropical basin case, Figs. 7 and 9, respectively. The initial anomaly (Fig. 12a) is the same as in Fig. 7a. The snapshots at 180, 360, and 540 days are plotted in Figs. 12b, 12c, and 12d, respectively. In spite of strong inertial–gravity waves, the large-scale pattern in each hemisphere is characterized by a narrow western boundary region due to the short Rossby wave, a widespread equatorial region due to equatorial waves, a widespread region of EBP, and a poleward boundary region of coastal Kelvin waves.

The evolution of the monthly mean SSH associated with the ECKC is plotted on the equator (h_{EQ}), the eastern (h_{EB}), and northern (h_{NB}) boundaries (Fig. 13). The three SSH time series show virtually the same amplitude and phase, as in the case of the extratropical basin, in Fig. 9a. However, different from Fig. 9a, the coastal SSH along the western boundary (not shown) is much larger than the others. One possible explanation is that the mass flux of the western boundary coastal Kelvin wave, which is trapped in a western boundary layer in the extratropics (tens of kilometers), is spread onto the equatorial Kelvin wave, which has a much wider equatorial deformation radius ($d_{EQ} \approx 300$ km).

Fortunately, as in an extratropical basin, the western-boundary Kelvin wave contributes little to the total mass redistribution

and therefore has little impact on the modulation of the ECKC.

The amplitude of the ECKC (multiplied by 10 in Fig. 13a) is about an order smaller than in the extratropical basin in Fig. 9a. This is due to the mass spreading over a much larger area, which now includes a large equatorial region and the Southern Hemisphere. As for Fig. 9, the end time for the initial pulse is about 360 days, both from the theory and the proxy time series of the incident wave (Fig. 13a, dot). However, the time of maximum ECKC is achieved at about day 270, in Fig. 13a, almost 100 days later than in Fig. 9a. This is consistent with the analysis above. The fast ECKC, which is dominated by the fast equatorial region, has a much larger area than the CKC in the extratropical basin. Therefore, the mass balance is more like the fast balance (29) than the slow balance in (26). Indeed, the mass evolution diagram in Fig. 13b clearly shows that much of the western-boundary incident mass (M_W) is rapidly injected into the ECKC ($M_N + M_S + M_{EQ}$) due to the fast redistribution. The EBP (M_E) never becomes comparable to the ECKC except at the very latest stage. This is in sharp contrast to the extratropical basin case (Fig. 9b), where the EBP is the dominant mass sink. The relatively greater importance of the ECKC can also be seen in the energy evolution diagram in Fig. 13c. In contrast to the extratropical basin case (Fig. 9c), the energy in the ECKC ($E_N + E_S + E_{EQ}$) is much stronger than the EBP (E_E) until after the end time.

Most of the ECKC energy is now APE (Fig. 13c). This is different from Fig. 9c. The reason is that the fast process in the equatorial region is dominated by low-latitude Rossby waves, rather than the equatorial Kelvin wave. Indeed, (33) gives the width of the fast equatorial region as $y_E = f(30^\circ) \times (10^\circ/20^\circ)^{1/2} \approx 20^\circ$. This is much wider than the equatorial deformation radius, $d_{EQ} \approx 3^\circ$, which is also the width of the equatorial Kelvin wave. To further examine the relative contribution of each subregion within the equatorial region, the equatorial region is subdivided into four bands: $|y| \leq 5^\circ$, $5^\circ < |y| \leq 10^\circ$, $10^\circ < |y| \leq 15^\circ$, and $15^\circ < |y| \leq 20^\circ$. The evolution of mass and energy in each band is plotted in Figs. 14a and 14b, respectively. It is seen that each band contributes about the same amount of mass and energy. The mass and energy of the two bands within 10° of latitude peak earlier at about day 220, while the other two bands peak later at day 300 and day 360. All these peaks occur before the end time T_{EI} (~ 360 days) and therefore represent the fast process.

For a quantitative comparison between our QG theory and the shallow-water experiments, two modifications are needed for our QG solution (11)–(14). First, the coastal Kelvin wave solution on the equatorial boundary (12) should be replaced with the width of y_E in (33), representing the fast equatorial region. Second, the areas of both the EBP and ECKC should be doubled to take into account the Southern Hemisphere. The amplitude of the ECKC can be derived from the same equation as the CKC in (25), except that the coefficients a and b in (23) need to be replaced by

$$\begin{aligned} b &= 2Yx_p / \{ \pi [2X(d + y_E) + Y\delta] \}, \\ a &= m_0 / \{ 2[2X(d + y_E) + Y\delta] \}. \end{aligned} \quad (34)$$

For the shallow-water example in Figs. 12–14, the modified QG theoretical solution produces ECKC amplitude in Fig. 15a (solid line). The maximum amplitude is $K_M = 0.039$, which is achieved at the time $T_M = 0.9$. This is in good agreement with the shallow-water solution (Fig. 13a), which has the normalized $K_M \approx 0.036$ and $T_M \approx 0.80$. The theoretical mass redistribution (Fig. 15b) also resembles the shallow-water solution (Fig. 13b) remarkably well. To examine the role of the fast mass balance (29) in determining the modulation of ECKC, the area ratio parameter can be calculated from (34) as $b \approx 0.3$. Therefore, the fast process is dominant in modulating the ECKC. This can be seen in Fig. 15a from the strong resemblance between the $K(T)$ with (solid) and without (dashed) the EBP. The mass exchange diagram (Fig. 15b) also resembles that without EBP in Fig. 15c except in the later stage. This resemblance becomes much clearer if one recalls the larger differences between Figs. 4b and 4c for the extratropical basin.

If the initial pulse is located closer to the equator [smaller Y_c in (33)], the width of the fast equatorial region shrinks [smaller y_E according to (33)], while the latitudinal width of the EBP increases (larger Y). Therefore, the area increases for the EBP, but decreases for the ECKC. The maximum amplitude of ECKC should, therefore, decrease and the time of that maximum should occur earlier. This is confirmed by three shallow-water sensitivity experiments in Fig. 16a, which plots the SSH averaged along the equator and outside the western boundary layer. One experiment is the same as in Figs. 12 and 13, with $Y_c = 30^\circ\text{N}$. The other two experiments have $Y_c = 25^\circ\text{N}$ and 20°N . Equation (33) gives the widths of the fast equatorial region as $y_E \approx 20^\circ$, 17.5° , and 14° , respectively. Figure 16a shows that the maximum amplitude K_M increases from about 0.036 to 0.042 and 0.048. The time for maximum (T_M) tends to decrease only slightly from about $0.8T_{EI}$. In comparison, the theoretical solution in Fig. 17a shows that K_M increases from 0.039 to 0.043 and 0.048, while T_M decreases slightly from $0.9T_{EI}$ to $0.88T_{EI}$ and $0.86T_{EI}$. The agreement is good, especially on the amplitude.

Finally, the mass evolution also agrees well between the model and theory (Figs. 16b and 17b). As Y_c moves toward the equator, the mass controlled by the fast process decreases, while the mass in the slow process increases. Correspondingly, the time of the maximum ECKC also becomes earlier. All these features can be understood from a stronger influence of the fast process of ECKC in the case with a Y_c closer to the equator. Thus, the modified QG theory is able to capture the major features of ECKC modulation. In contrast to an extratropical basin, the most important mass redistribution mechanism in a combined extratropical–tropical basin, becomes the fast equatorial waves. Consequently, the time of maximum ECKC is delayed substantially, approaching the end time of the incident wave. The maximum amplitude is usually small.

5. Summary and discussions

The adjustment of a midlatitude ocean basin to a planetary wave packet incident onto the western boundary is studied both analytically and numerically. The focus is on the low-frequency modulation of the resulting coastal Kelvin wave. This coastal Kelvin wave, at low frequencies, can be approximated as a coastal Kelvin wave current (CKC) along the boundaries of the basin. It is shown that the CKC is modulated mainly by two mass redistribution processes: a fast process due to the CKC, and a slow process due to the eastern boundary planetary wave (EBP). Because the mass is eventually redistributed to a much larger area of basin scale, the amplitude of the CKC is usually much smaller than that of the initial disturbance. In a midlatitude basin, the EBP dominates mass redistribution, which results in a Kelvin wave peak time close to that of the incident wave. The short Rossby wave, although contributing little to mass redistribution, absorbs most energy at the western boundary.

The QG theory is further extended to a combined extratropical–tropical basin. Now, the fast equatorial waves, both Kelvin and Rossby waves, form the equatorial coastal Kelvin wave current (ECKC) and dominate mass redistribution. As a result, the coastal Kelvin wave peaks near the end time of the incident wave.

a. Rossby–Kelvin wave interaction in the midlatitude and equatorial regions

It is interesting to compare our results of Rossby–Kelvin wave interaction in the midlatitude with that in the equatorial region (Cane and Sarachik 1977, 1979). In both cases, mass redistribution is the major constraint for the interaction. However, significant differences exist. First, the reflection of equatorial Kelvin and Rossby waves is constrained by the balance of cross-shore mass flux at the coast. In the midlatitudes, however, the coastal Kelvin wave is generated to balance the alongshore mass flux of the incident long wave, while the cross-shore mass flux is completely balanced by the reflected short Rossby wave. Second, the equatorial Kelvin wave and low mode Rossby waves have comparable wave speeds, while the midlatitude Rossby wave is far much slower than the coastal Kelvin wave. This has several consequences. First, the equatorial interaction is a local process. In the midlatitudes, however, the interaction depends critically on the remote area that is affected by the coastal Kelvin wave during the slow modulation time. Given an incident long wave, the coastal Kelvin wave evolves differently for various basins, as seen in the cases of the midlatitude and extratropical–tropical basins (compare Figs. 7 and 12). A closed basin also differs from a half-plane ocean, in the latter of which Kelvin waves eventually diminish because of the ever expanding coastal area (Dorofeyev and Larichev 1992). Second, the comparable speed of equatorial waves implies that the incident and reflected waves occupy about the same area and therefore both have a comparable amplitude. Therefore, the reflected wave can balance not only the mass but also the energy fluxes of the incident wave. In the midlatitudes, however, the coastal Kelvin wave is important for mass balance, but not for energy balance. The latter is accomplished by reflected short Rossby waves. Indeed, regardless of mass conservation (or the consistency condition of McWilliams 1977), the QG system conserves energy within a closed basin. Third, the comparable speed and local reflection nature of the equatorial waves also ensures that both incident and reflected waves always peak at the same time. For an incident midlatitude Rossby wave, however, the resulting coastal Kelvin wave could peak at different times, depending on the basin. In a midlatitude basin, the coastal Kelvin wave does peak around the same time as the incident Rossby wave did at the western boundary. However, when the equator is present in the basin, the coastal Kelvin wave peaks substantially later.

b. Extratropical–tropical wave interaction

Our study suggests that an extratropical thermocline anomaly can modulate the mean equatorial thermocline through the ECKC. However, the resulted equatorial thermocline anomaly is usually much smaller than the initial extratropical anomaly. Nevertheless, a large-scale anomaly at a relatively low latitude may still produce a non-negligible anomaly in the equatorial region. This seems to agree qualitatively with the numerical experiment of Lysne et al. (1997). The equatorial thermocline temperature anomaly that is transmitted by the western boundary coastal Kelvin wave is about 0.2°C (in comparison, their modeled subduction anomaly can reach 1°C in the extratropics). These anomalies, although small, could be amplified by positive ocean–atmosphere feedbacks and therefore may still be important for climate variability.

One alternative way of thinking may also be helpful in understanding extratropical–tropical interaction (Battisti 1989, 1991;

[Kessler 1991](#)). In terms of the classical theory of equatorial wave (latitudinal) modes, an extratropical long Rossby wave packet could have significant projection on some higher mode equatorial Rossby waves, whose turning latitudes, and in turn the maximum pressure anomalies, are located in the extratropics. For example, mode 15 has the peak pressure at about latitude 17° ([Fig. 1](#) of [Kessler 1991](#)). The reflected Kelvin wave, calculated by zonal mass flux balance, has a small amplitude, less than 10% of the incident wave ([Fig. 3](#) of [Kessler 1991](#)). The afterward equatorial wave adjustment should have an amplitude comparable to this equatorial Kelvin wave. Qualitatively, this small amplitude of equatorial response is consistent with our conclusion in [section 4](#). This modal approach easily produce the first reflection equatorial Kelvin wave, but it is not convenient to describe the low-frequency modulation of the equatorial thermocline, which is accomplished after multireflection in the equatorial wave guide. The modal approach is also inconvenient to describe a temporal adjustment process. For example, it is difficult to obtain the timing of maximum modulation of equatorial thermocline. Indeed, it gives the timing of the first reflection equatorial Kelvin wave the same as the incident Rossby wave, which is earlier than the peak time of the modulated equatorial thermocline. In addition, a higher mode of equatorial Rossby wave, although having a pressure peak in the extratropics, has significant, alternating zonal velocity all the way to the turning latitude ([Fig. 2](#) of [Kessler 1991](#)); these higher modes are also very dispersive. Therefore, strictly speaking, any single high mode is difficult to represent a nondispersive planetary wave packet localized in the midlatitude. Finally, the modal approach still uses zonal mass flux balance, while our approach uses alongshore mass flux balance. In spite of these differences, the modal approach and our approach could still be complementary to each other.

Our study may have important implication to the understanding of general oceanic circulation and its low-frequency variability. Past attention has focused on Rossby waves. Our study shows that the coastal Kelvin wave is an inseparable part of the general circulation system especially for low-frequency variability. The associated CKC could be of critical importance in determining the boundary pressure distribution of the general circulation, which in turn affects the interior ocean. In an accompany paper ([Liu et al. 1999](#)), our theory is extended to study the variability of the general circulation around an island ([Godfrey 1989](#)). The interaction between the coastal Kelvin wave and Rossby waves, especially the short Rossby waves, will be seen as critical elements in the establishment of the island circulation. This effect of short Rossby wave is reminiscent of the wave interaction on an equatorial island ([Cane and du Penhoat 1982](#)).

Our study so far remains preliminary. Many important processes need to be studied in order to gain a full understanding of the realistic ocean. One limitation of the present work is the linear wave assumption. In the real ocean such as the North Pacific, the main thermocline tends to outcrop at mid- and high latitude. As a result, a Kelvin wave may not be able to propagate around the basin. We speculate that this latitudinal constraint of the Kelvin wave propagation will not change the major features of our work here. This is because, in our theory, the polar boundary plays a negligible role in both the mass and energy balance. The reduction of the latitudinal extent of the eastern boundary Rossby wave, however, may result in a larger amplitude of the Kelvin wave because the initial mass is redistributed onto an area smaller than the entire basin. This speculation remains to be investigated. A study of the effect of the mean flow advection is also in progress. The adjustment in a realistic Pacific Ocean is also under current study (Wu and Liu 1999, manuscript submitted to *J. Phys. Oceanogr.*). Our preliminary results suggest that the simple theory here can be applied successfully to understanding the interaction of open ocean with the western coastal Pacific Ocean and its marginal seas, as well as the equatorial Pacific Ocean.

Acknowledgments

We would like to thank Dr. P. Chang for a discussion on extratropical–tropical interaction, which provided a strong motivation for this work; Drs. J. A. Young and H. Hurlburt for helpful discussions in the early stage of the work; Dr. J. McCreary for his comments on an early version of the paper; and Dr. J. S. Godfrey for bringing our attention to his early relevant work during our revision. We also thank Dr. A. Wallcraft for his help in the set up of the shallow-water model. Comments from two anonymous reviewers have helped to improve the paper substantially. This work is supported by ONR, NSF, and NOAA. The calculation of the shallow-water model is performed on the supercomputer at the Stennis Space Center, which is supported by ONR.

REFERENCES

- Anderson, D. L. T., and A. E. Gill, 1975: Spin-up of a stratified ocean with applications to upwelling. *Deep-Sea Res.*, **22**, 583–596..
- Battisti, D. S., 1989: On the role of off-equatorial oceanic Rossby waves during ENSO. *J. Phys. Oceanogr.*, **19**, 551–559.. [Find this article online](#)
- , 1991: Reply. *J. Phys. Oceanogr.*, **21**, 461–465.. [Find this article online](#)
- Cane, M. A., and E. S. Sarachik, 1977: Forced baroclinic ocean motions. II. The linear equatorial bounded case. *J. Mar. Res.*, **35**, 395–432..
- , and —, 1979: Forced baroclinic ocean motions. III. The linear equatorial basin case. *J. Mar. Res.*, **37**, 355–398..

- , and D. Moore, 1981: A note on low frequency equatorial basin modes. *J. Phys. Oceanogr.*, **11**, 1578–1584.. [Find this article online](#)
 - , and Y. du Penhoat, 1982: The effect of islands on low frequency equatorial motions. *J. Mar. Res.*, **40**, 937–962..
 - , and S. E. Zebiak, 1985: A theory for El Nino and the Southern Oscillation. *Science*, **228**, 1084–1087..
- Dorofeyev, V. L., and V. D. Larichev, 1992: The exchange of fluid mass between quasi-geostrophic and ageostrophic motions during the reflection of Rossby waves from a coast. I. The case of an infinite rectilinear coast. *Dyn. Atmos. Oceans*, **16**, 305–329..
- Enfield, D., and J. Allen, 1980: On the structure and dynamics of monthly mean sea level anomalies along the Pacific coast of North and South America. *J. Phys. Oceanogr.*, **10**, 557–578.. [Find this article online](#)
- Flierl, G. R., 1977: Simple applications of McWilliams' A note on a consistent quasigeostrophic model in a multiply-connected domain. *Dyn. Atmos. Oceans*, **1**, 443–453..
- Fofonoff, N. P., 1954: Steady flow in a frictionless homogeneous ocean. *J. Mar. Res.*, **13**, 254–262..
- Godfrey, J. S., 1975: On ocean spindown. I: A linear experiment. *J. Phys. Oceanogr.*, **5**, 399–409.. [Find this article online](#)
- , 1989: A Sverdrup model of the depth-integrated flow from the world ocean allowing for island circulations. *Geophys. Astrophys. Fluid Dyn.*, **45**, 89–112..
- Jacobs, G. A., H. E. Hurlburt, J. C. Kindle, E. J. Metzger, J. L. Mitchell, W. J. Teague, and A. G. Wallcraft, 1994: Decade-scale trans-Pacific propagation and warming effects of an El Nino anomaly. *Nature*, **370**, 360–363..
- Kawase, M., 1987: Establishment of deep ocean circulation driven by deep-water production. *J. Phys. Oceanogr.*, **17**, 2294–2317.. [Find this article online](#)
- Kessler, W. S., 1991: Can reflected extra-equatorial Rossby waves drive ENSO? *J. Phys. Oceanogr.*, **21**, 444–452.. [Find this article online](#)
- Liu, Z., 1990: On the influence of the continental slope on the inertial western boundary current—the enhanced transport and recirculation. *J. Mar. Res.*, **48**, 254–284..
- , L. Wu, and H. Hurlburt, 1999: Rossby wave–coastal Kelvin wave interaction. Part II: Formation of island circulation. *J. Phys. Oceanogr.*, **29**, 2405–2418.. [Find this article online](#)
- Lysne, J., P. Chang, and B. Giese, 1997: Impact of the extratropical Pacific on equatorial variability. *Geophys. Res. Lett.*, **24**, 2589–2592..
- McCalpin, J. D., 1995: Rossby wave generation by poleward propagating Kelvin waves: The midlatitude quasigeostrophic approximation. *J. Phys. Oceanogr.*, **25**, 1415–1425.. [Find this article online](#)
- McCreary, J., 1976: Eastern tropical ocean response to changing wind systems with application to El Niño. *J. Phys. Oceanogr.*, **6**, 632–645.. [Find this article online](#)
- , 1983: A model of the tropical ocean–atmosphere interaction. *Mon. Wea. Rev.*, **111**, 370–387.. [Find this article online](#)
 - , and P. Kundu, 1988: A numerical investigation of the Somali Current during the southwest Monsoon. *J. Mar. Res.*, **46**, 25–58..
- McWilliams, J. C., 1977: A note on a consistent quasi-geostrophic model in a multiply-connected domain. *Dyn. Atmos. Oceans*, **1**, 427–441..
- Miles, J. W., 1972: Kelvin waves on oceanic boundaries. *J. Fluid Mech.*, **55**, 113–127..
- Milliff, R. F., and J. C. McWilliams, 1994: The evolution of boundary pressure in ocean basins. *J. Phys. Oceanogr.*, **24**, 1317–1338.. [Find this article online](#)
- Pedlosky, J., 1965: A note on the western intensification of the oceanic circulation. *J. Mar. Res.*, **23**, 207–210..
- , 1987: *Geophysical Fluid Dynamics*. Springer-Verlag, 710 pp..
 - , L. J. Pratt, M. A. Spall, and K. R. Helfrich, 1997: Circulation around islands and ridges. *J. Mar. Res.*, **55**, 1199–1251..
- Wallcraft, A. J., 1991: The navy layered ocean model users guide. NOARL Rep. 35, Stennis Space Center, MS, 21 pp..
- White, W., and J. Saur, 1983: Sources of interannual baroclinic waves in the eastern subtropical North Pacific. *J. Phys. Oceanogr.*, **13**, 531–544.. [Find this article online](#)

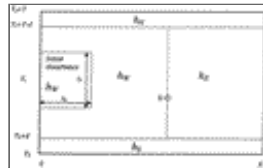
APPENDIX

6. Wave Interaction around an Island

The basin solution (25) can be applied directly to an island of the size X and Y , shown schematically in [Fig. A1](#). The incident wave now hits the east coast of the island ($x = X_I + X$), producing a CKC around the northern ($y = Y_I + Y$), western ($x = X_I$), and southern ($y = Y_I$) boundaries of the island. A new planetary wave is radiated westward from the west coast of the island (corresponding to the EBP in the basin case, and thus will still be called the EBP). Solution (25) is valid until the EBP hits the western boundary of the basin (at $x = 0$) or $t < X_I/C$. All the discussions on the modulation of the amplitude of CKC, the mass exchange, and energetics will be the same as in the QG theoretical basin solution. Furthermore, later adjustment after the EBP hits the western boundary of the basin can also be discussed similarly, if one replaces the basin size with $X_B \times Y_B$ and the incident wave packet size with $x_p \times Y$.

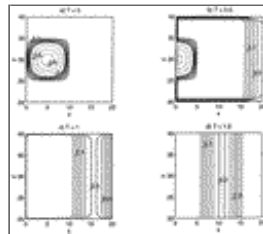
[Figure A2](#) shows one example of SSH snapshots in a basin including an island. The evolution is essentially the same as that in a basin ([Fig. 2](#)). The corresponding shallow-water experiment is shown in [Fig. A3](#), whose mass and energy evolution are shown in [Figs. A4a and A4b](#), respectively. The agreement of the mass evolution [Figs. A4a](#) and the theoretical solution (the same as [Fig. 4b](#)) is remarkable. Indeed, the agreement is better than the basin case of the shallow-water experiment ([Fig. 9b](#)). For example, the overestimation of the CKC mass component in the basin case in [Fig. 9b](#), compared with the theory, [Fig. 4b](#), virtually disappeared in the island shallow-water experiment ([Fig. A4b](#)). Correspondingly, the energetics ([Fig. A4c](#)) also show a better agreement with the theory ([Fig. 6](#)) than the basin shallow-water case ([Fig. 9c](#)). The reason is simple. In the island case, the EBP does not interact with the northern and southern boundaries of the basin, even in the shallow-water model. This is the case of the QG theoretical basin solution (25), which has neglected the Kelvin wave produced by the EBP on the northern and southern boundaries. However, in a basin model, either QG or shallow water, the EBP will interact with the northern and southern boundaries, generating additional Kelvin waves.

Figures



[Click on thumbnail for full-sized image.](#)

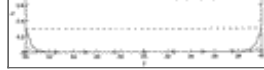
Fig. 1. Schematic figure of an extratropical basin: various solution regimes for the adjustment process are plotted. The initial planetary wave is plotted in solid lines against the western boundary. The dashed lines separate the basin solution into western (h_W), southern (h_S), eastern (h_E), and northern (h_N) regions.



[Click on thumbnail for full-sized image.](#)

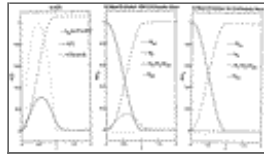
Fig. 2. Four snapshots of the analytical solution in Eqs. (11)–(14). (a) Initial condition, (b) $T = 0.5$, the peak time of the initial long wave, (c) $T = 1$, the end time of the initial long wave, and (d) $T = 1.5$. The contour interval is 0.05 for the solid lines and 0.2 for the dotted lines.





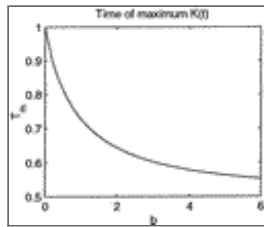
Click on thumbnail for full-sized image.

Fig. 3. Sea surface height profiles of the snapshots in Fig. 2 along (a) the zonal section of the middle basin latitude, $y = 30^\circ$ N, and (b) the meridional section of the middle basin longitude, $x = 10^\circ$.



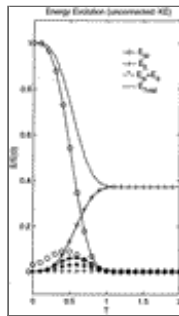
Click on thumbnail for full-sized image.

Fig. 4. (a) Evolution of the amplitudes for the Kelvin wave $K(T)$ with (solid line) and without ($b = 0$, dashed line) the EBP and the magnitude of the incident long wave at $x = 0^\circ$, $y = 30^\circ$ N (dotted line). (b) The evolution of each mass component of the solution with the EBP [solid line in (a)]. (c) The evolution of each mass component of the solution without the EBP [dashed line in (a)]. The definitions for each mass component are [Eqs. (17)–(21)] M_{WL} , incident long wave; M_E , eastern boundary planetary wave; M_N , northern boundary Kelvin wave; M_S , southern boundary Kelvin wave; M_{WK} , western boundary Kelvin wave and the resulting short Rossby wave; and M_{WS} , damped western boundary short Rossby wave. Both the amplitude and mass are normalized by the initial perturbation amplitude.



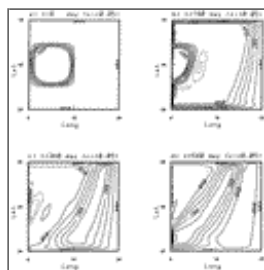
Click on thumbnail for full-sized image.

Fig. 5. The time for maximum Kelvin wave amplitude (T_M) as a function of the area ratio parameter b [defined in (23)]. Friction is neglected in this case ($q = 0$).



Click on thumbnail for full-sized image.

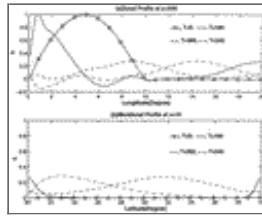
Fig. 6. Energy evolution for different basin regions (Fig. 1): the western region (E_W , circle marked), the eastern region (E_E , plus marked), and the northern and southern regions ($E_N + E_S$, star marked). The total energy is also plotted (E_{Total} , solid). Kinetic energy for each region is indicated by symbols without line connection.



Click on thumbnail for full-sized image.

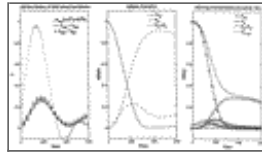
Fig. 7. Four snapshots of sea surface height of the shallow-water experiment (normalized by the initial perturbation amplitude) at (a) initial time, (b) $t = 0.5T_{EI}$, (c) $t = T_{EI}$, and (d) $t = 1.5T_{EI}$ where T_{EI} is the end time of the initial planetary wave (360 days).

Contour interval is 0.05. Contours larger than 0.4 are not plotted.



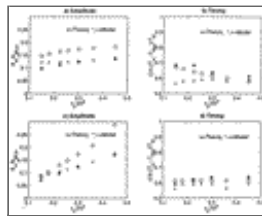
Click on thumbnail for full-sized image.

Fig. 8. Normalized sea surface height profiles for the shallow-water solution snapshots in Fig. 7, along (a) the middle basin latitude $y = 30^\circ\text{N}$, and (b) the middle basin longitude $x = 10^\circ$.



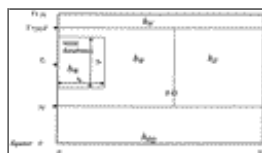
Click on thumbnail for full-sized image.

Fig. 9. (a) Evolution of coastal sea surface heights on the eastern (h_{EB} , star), southern (h_{SB} , solid), northern (h_{NB} , plus), and western (h_{WB} , circle) boundaries (in the middle of each boundary). These sea surface heights can be taken as the proxies for the Kelvin wave amplitude $K(t)$ in the theoretical QG solution. The proxy time series of the incident long wave at the west coast [h_{WL} ($x = 0^\circ$, $y = 30^\circ\text{N}$), dot] is calculated using the sea surface height outside the western boundary layer ($x = 0.6^\circ$, $y = 30^\circ\text{N}$) by adding a time offset of $0.6^\circ/C$. (b) The mass evolution in the western region M_W , eastern region M_E , and the combined northern and southern boundary region $M_N + M_S$ (see Fig. 1). The boundary of the western and eastern regions change with time as in Fig. 1 to track the planetary wave packets. For comparison with the theoretical results in Fig. 4, the nondimensional time $T = 1$ there corresponds to the dimensional time of about 360 days.



Click on thumbnail for full-sized image.

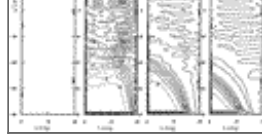
Fig. 10. Shallow-water sensitivity experiments on the size (x_p and y_p) and location of the initial planetary wave packet. The normalized maximum amplitude K_M (a), (c) and time of maximum amplitude T_M (b), (d) are plotted against the different zonal (a), (b) and meridional (c), (d) dimensions. (a) and (b) Two sets of experiments with different zonal widths (x_p): one set of seven experiments (pluses) have the initial perturbation patch centered in the middle of the basin, while the other set of four experiments (stars) have the west edge of the initial pulse on the western boundary. All 11 cases have the same $y_p = 6^\circ$. The maximum amplitude in (a) is normalized by the maximum derived from the time series of SSH outside the western boundary layer $h(0.8^\circ, 30^\circ\text{N})$, while the time for maximum in (b) are normalized by the theoretical end time $T_{EI} = x_p/C$. The QG theoretical solutions are also plotted (circles). (c) and (d) Same as (a) and (b), except that the experiments have different meridional dimensions while using the same zonal width $x_p = 6^\circ$.



Click on thumbnail for full-sized image.

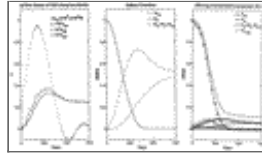
Fig. 11. The schematic figure of different solution regimes in a combined extratropical–tropical ocean basin. Compared with an extratropical basin, the equatorial region replaces the equator-side coastal Kelvin wave region.





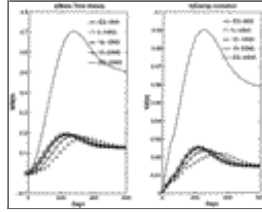
Click on thumbnail for full-sized image.

Fig. 12. As in Fig. 7 but in a combined extratropical–tropical basin. Now, the contour interval is 0.005 (label scaled by 1000), and contours above 0.1 are not plotted.



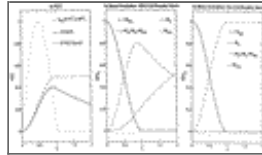
Click on thumbnail for full-sized image.

Fig. 13. Similar to Fig. 9 but for the combined extratropical–tropical basin case in Fig. 12. (a) Evolution of boundary sea surface heights multiplied by a factor 10: along the equator (h_{EQ} , solid), northern boundary (h_{NB} , dash), and eastern boundary (h_{EB} , dash–dot). The western coastal sea surface height is not plotted. The dot is the proxy for the incident long wave amplitude calculated from the sea surface height outside the western boundary at $(0^\circ, 30^\circ N)$ (similar to Fig. 9). (b) Mass evolution and (c) energy evolution. The fast process region now consists of the northern boundary, southern boundary, and the equatorial region. The equatorial region has the latitude span $y_E = 20^\circ$, as calculated from Eq. (33).



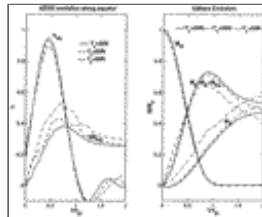
Click on thumbnail for full-sized image.

Fig. 14. The mass (a) and energy (b) evolution in each subequatorial region (5° latitude in both hemispheres) for the case of Fig. 12. The mass (energy) from both hemispheres, within the specified bond, is combined in the plotted totals.



Click on thumbnail for full-sized image.

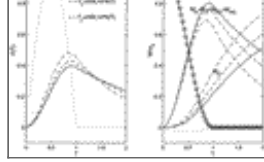
Fig. 15. Evolution of the QG theoretical solution: same as in Fig. 4 but uses the modified theoretical QG solution [Eqs. (25) and (34)] to simulate the case in a combined extratropical–tropical basin (Fig. 12). The $b = 0$ case is without the EBP.



Click on thumbnail for full-sized image.

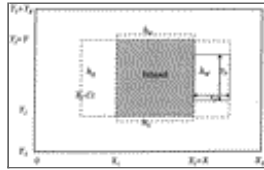
Fig. 16. Three shallow-water sensitivity experiments in the combined extratropical–tropical basin with different center latitudes $Y_c = 30^\circ N$ (solid), $25^\circ N$ (dash), and $20^\circ N$ (dash–dot) for the initial planetary wave patch. (a) The evolution of the zonal mean equatorial sea surface height (h_{EQ} , multiplied by 10) and the proxy of incident long wave sea surface height calculated from the sea surface height outside the western boundary layer at $(0.6^\circ, 30^\circ N)$. Time is normalized by the end time of each corresponding initial patch. (b) The evolution of mass of the western (M_W), eastern (M_E), and the combined equatorial, northern and southern boundary regions ($M_N + M_S + M_{EQ}$).





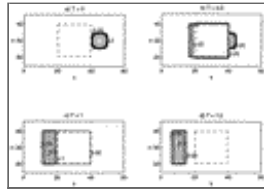
Click on thumbnail for full-sized image.

Fig. 17. As in [Fig. 16](#) but for the modified QG theoretical solution of (25) and (34): (a) $K(t)$ (multiplied by 10) and sea surface height on the west coast (dot); (b) the mass evolution.



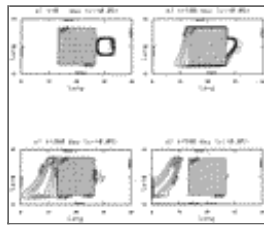
Click on thumbnail for full-sized image.

Fig. A1. Schematic figure of different solution regimes for an initial planetary wave incident on the east coast of an island.



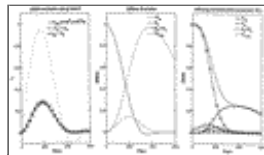
Click on thumbnail for full-sized image.

Fig. A2. Four snapshots of the theoretical QG solution, similar to [Fig. 2](#), but for the corresponding island case.



Click on thumbnail for full-sized image.

Fig. A3. Four snapshots of a shallow-water experiment, similar to [Fig. 7](#), but for the corresponding island case.



Click on thumbnail for full-sized image.

Fig. A4. The same as in [Fig. 9](#) but of the shallow-water experiment for the corresponding island case. The notation of the solution regime is the same as in [Fig. A1](#) with subscripts “W” for the region east of the island and “E” for the region west of the island.

¹ All major conclusions can be derived in a generalized QG equation and are independent of the form of dissipation. More specifically, the solution along the eastern boundary in a generalized QG equation has been derived in [McCalpin \(1995\)](#). The solution along the western boundary in a generalized QG equation is derived in [Liu et al. \(1999\)](#), which is also similar to [Godfrey \(1975\)](#).

² The effect of the Kelvin wave on the eastern boundary is always much smaller than the EBP and therefore will not be discussed separately.

³ The equatorial deformation radius d_{EQ} is the latitude where the speeds of the equatorial Kelvin wave and extratropical Rossby wave equal each other: $(g'D)^{1/2} = \beta g'D/f^2(d_{EQ})$.



© 2008 American Meteorological Society [Privacy Policy and Disclaimer](#)
Headquarters: 45 Beacon Street Boston, MA 02108-3693
DC Office: 1120 G Street, NW, Suite 800 Washington DC, 20005-3826
amsinfo@ametsoc.org Phone: 617-227-2425 Fax: 617-742-8718
[Allen Press, Inc.](#) assists in the online publication of *AMS* journals.